An ALE Finite Element Method for Baffled Fuel Container in Yawing Motion

Jin-Rae Cho*, Hong-Woo Lee, Wan-Suk Yoo, Min-Jeong Kim
School of Mechanical Engineering, Pusan National University, Pusan 609-735, Korea

A computational analysis of engineering problems with moving domain or/and boundary according to either Lagrangian or Eulerian approach may encounter inherent numerical difficulties, the extreme mesh distortion in the former and the material boundary indistinctness in the latter. In order to overcome such defects in classical numerical approaches, the ALE (arbitrary Lagrangian Eulerian) method is widely being adopted in which the finite element mesh moves with arbitrary velocity. This paper is concerned with the ALE finite element formulation, aiming at the dynamic response analysis of baffled fuel-storage container in yawing motion, for which the coupled time integration scheme, the remeshing and smoothing algorithm and the mesh velocity determination are addressed. Numerical simulation illustrating theoretical works is also presented.

Key Words : ALE Finite Element Method, Coupled Iterative Time Integration, Remeshing and Smoothing, Newmark and Fractional Methods, Baffled Fuel Container

1. Introduction

In the computational mechanics community, the numerical analysis and design of the dynamic problems characterized by the significant time-varying domain had become a great challenging research subject during several decades. Needless to say, it is because traditional two basic approaches in describing kinematics of problem, Lagrangian and Eulerian, could not successfully deal with both of the excessive mesh distortion and the material boundary indistinctness at the same time. In other words, the excessive mesh distortion in the Lagrangian approach causes either long CPU time or instability in numerical computation, while the material boundary indistinctness in the latter approach makes the boundary identification be a hard task.

These numerical difficulties can be completely and effectively resolved by employing the arbitrary Lagrangian-Eulerian approach. According to our research survey, this kinematic description concept was introduced originally by Hirt et al. (1974) for the finite difference method. But it has been extended to the finite element method by numerous investigators such as Belytschko and Kennedy (1978), Hughes et al.(1981), Donea et al.(1982) and Benson (1989). The prominent feature of this approach is the arbitrary movement of finite element mesh differing from the material velocity. Being defined as a third coordinates (or a reference domain) additional to usual spatial and material coordinates, the finite element mesh is adjusted according to a selective combination of remeshing and smoothing processes, in order to keep the mesh regularity and track down the material boundary exactly. Hence, the numerical techniques associated with the determination of the finite element mesh velocity should be accompanied, despite of the term "arbitrary".

* Corresponding Author,
E-mail : jrcho@hyowon. pusan.ac.kr
TEL : +82-51-510-2467; **FAX** : +82-51-514-7640
School of Mechanical Engineering, Pusan National University, Pusan 609-735, Korea. (Manuscript **Received** August 29, 2003; **Revised** January 5, 2004)

In connection with the advances in computational techniques, the dynamic response analysis of fuel-storage containers of vehicles such as automobiles and aircrafts, while being a representative research topic in fluid-structure interaction, has become a major application problem of the ALE numerical method. In fact, the structural dynamic behavior of such containers is characterized by the strong dynamic coupling between the structure deformation and the complicated fluid flow (Paidoussis, 1998; Cho and Song, 2001). However, early studies (Abramson, 1966; Bauer, 1966) before the introduction of the ALE method) were quite restricted so that the reliable and profound dynamic analysis was not possible.

Meanwhile, the structural stability of fuel containers in moving vehicles is greatly affected by the hydrodynamic forces by internal fuel flow. Hence, most of research efforts have focused on how to effectively suppress the hydrodynamic force, and several kinds of dynamic damping devices were introduced (Miyata et al., 1988; Welt and Modi, 1992). Among them, a metallic baffle has been reported to be most suitable from a practical and installation point of view. And, the design of baffled fuel container is performed based upon the parametric investigation of structural dynamic characteristics to the design variables such as the number and the inner-hole size of baffles. From the computational analysis point of view, however the dynamic analysis of baffled case requires more sophisticated techniques, owing to the complex fuel flow, like the ALE finite element method.

In this paper, we intend to present an ALE finite element method for the structural dynamic analysis of baffled fuel container in yawing motion. Together with theoretical and numerical formulations, the core techniques in the ALE approach such as the remeshing and smoothing algorithms, the coupled fluid-structure time integration scheme and the stability criterion are addressed. As well, the numerical results of parametric characteristics of a baffled cylindrical fuel container in yawing motion to the major baffle parameter are given.

2. Problem Description in ALE Kinematic Description

Figure 1 shows a baffled cylindrical fuel container of uniform thickness t, with an elastic metal baffle of thickness t_B and inner-hole diameter D_B, in which incompressible viscous fuel is filled up to the height H_F. Throughout this paper, subscripts F and B refer to the parameters of fuel and baffle, respectively. As usual, the baffle is manufactured with the same material as the container, and the number and spacing, the inner-hole diameter and the thickness become the major design variables.

When adopting Cartesian coordinate system, the structural dynamic motion of the structure occupying the spatial domain Ω is governed by

$$\sigma_{ij}(\boldsymbol{u})_{,j}-c\frac{\partial u_i}{\partial t}=\rho\left(\frac{\partial^2 u_i}{\partial t^2}-g_i\right),\ \text{in}\ \Omega\times(0,\ T] \quad (1)$$

with initial and boundary conditions:

$$u_i(0)=\dot{u}_i(0)=0,\ \text{in}\ \Omega \quad (2)$$

$$u_i=\hat{u}_i,\ \text{on}\ \partial\Omega_D\times(0,\ T] \quad (3a)$$

$$\sigma_{ij}n_j=t_i,\ \text{on}\ \partial\Omega_t\times(0,\ T] \quad (3b)$$

Here, c, ρ and g_i indicate respectively the damping coefficient, the structure density and gravity acceleration components, while $\partial\Omega_D$ the displacement boundary region and $\partial\Omega_t$ the common fuel-structure interface. Meanwhile, the surface traction on the fuel-structure interface is $\boldsymbol{t}\cdot\boldsymbol{n}=-p$ by denoting p as the hydrodynamic pressure, and the external dynamic loading is acceleration-type yawing excitation.

On the other hand, the unsteady viscous flow of interior incompressible fuel occupying the time-

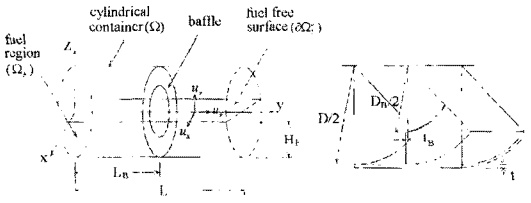

Fig. 1 Definition of geometry and symbols of baffled cylindrical fuel container

varying spatial domain $\Omega_F(t)$ is governed by the mass and momentum conservation laws. And, which are expressed in the ALE numerical approach such that

$$\frac{\partial v_i}{\partial t}+(v_j-\hat{v}_j)v_{i,j}-\frac{1}{\rho_F}\tau_{ij,j}=g_i, \text{ in } \Omega_F\times(0,\ T] \quad (4)$$

$$v_{i,i}=0, \text{ in } \Omega_F\times(0,\ T] \quad (5)$$

where v_i and ρ_F indicate the flow velocity components measured in the mesh referential coordinates $\boldsymbol{x}$ and the fuel density, respectively. In the ALE kinematic description, the convection term $v_jv_{i,j}$ in the momentum equations in Eulerian kinematics is substituted with $(v_j-\hat{v}_j)v_{i,j}$ according to the difference between the material velocity and the mesh velocity $\hat{\boldsymbol{v}}$ (Donea et al., 1982). By denoting the kinematic viscosity of fuel by μ, the stress tensor τ_{ij} is constituted as follows:

$$\tau_{ij}=\mu(v_{i,j}+v_{j,i})-p\delta_{ij} \quad (6)$$

The time-varying boundary $\partial\Omega_F(t)$ of the fuel domain is composed of the free surface $\partial\Omega_F^S$ and the fuel-structure interface $\partial\Omega_I$ such that $\partial\Omega_F=\overline{\partial\Omega_F^S\cup\partial\Omega_I}$. Then, the momentum equations are to be solved with the initial and boundary conditions given by

$$v_i(\boldsymbol{x},\ 0)=0, \text{ in } \Omega_F \quad (7)$$

$$v_i=\frac{\partial u_i}{\partial t}, \text{ on } \partial\Omega_I\times(0,\ T] \quad (8a)$$

$$\tau_{ij}n_j=\hat{t}_i, \text{ on } \partial\Omega_F^S\times(0,\ T] \quad (8b)$$

where $\hat{t}_i$ are the traction components acting on the fuel free surface.

The major difficulties in the time integration of the ALE flow equations (4) and (5) are caused by the presence of the convection term and the incompressibility constraint. Broadly speaking, there exist two methods to implement those according to conventional two approaches used in Eulerian fluid mechanics, the operator split method (Donea et al., 1982; Benson, 1989) and the fully coupled time integration method (Kennedy and Belytschko, 1981; Hughes et al., 1981).

In the former method, the time integration is divided into two phases, Lagrangian and Eulerian ones. Of course, the Lagrangian phase is solved first by neglecting the convection term, and then the necessity of mesh smoothing is examined. If needed, the Eulerian phase is followed in order to take the convection term due to the mesh smoothing into consideration. This method breaks a complex problem into simpler one and the second phase is not needed at all time stages, but the convection effect and the incompressibility are treated in a rather approximation manner.

On the other hand, a severe difficulty in the latter method is to get the flow velocity satisfying the incompressibility constraint. In order to resolve this problem, the fractional concept stemming from Chorin's method had been adopted. Where, the momentum equations (4) were solved first by introducing an intermediate velocity which does not satisfy the incompressibility condition, while decoupling the pressure gradient term from Eq. (4). After that, the intermediate velocity is corrected by the pressure obtained from the continuity equation (5). However, this correction process took remarkable numerical iterations for the converged velocity. This defect can be resolved by employing the C-fractional method proposed by Hayashi et al.(1991) which will be described later in details.

3. Finite Element Approximations

According to the principle of virtual work, we can obtain the weak form of Eq. (1), to which we introduce the isoparametric finite element approximation for the dynamic displacement $\boldsymbol{u}(\boldsymbol{x},\ t)=\boldsymbol{\Phi}(\boldsymbol{x})\cdot\bar{\boldsymbol{u}}(t)$ with denoting $\boldsymbol{\Phi}$ as the $(3\times3N)$ matrix in terms of N basis functions. Then, we arrive at the usual numerical system of equations given by

$$\boldsymbol{M}\ddot{\bar{\boldsymbol{u}}}+\boldsymbol{C}\boldsymbol{u}+\boldsymbol{K}\bar{\boldsymbol{u}}=\boldsymbol{F} \quad (9)$$

in which the load vector F is due to the body force and the hydrodynamic pressure.

Next, we do temporal discretization of Eq. (9) according to the implicit Newmark constant-averaged-acceleration method (Bathe, 1996) such that

$$\left[\boldsymbol{M}+\frac{\Delta t}{2}\boldsymbol{C}+\beta(\Delta t)^2\boldsymbol{K}\right]\ddot{\bar{\boldsymbol{u}}}^{n+1} = -\left[\frac{\Delta t}{2}\boldsymbol{C}+\left(\frac{1}{2}-\beta\right)(\Delta t)^2\boldsymbol{K}\right]\ddot{\bar{\boldsymbol{u}}}^{n} - [\boldsymbol{C}+\Delta t\cdot\boldsymbol{K}]\dot{\bar{\boldsymbol{u}}}^{n}-\boldsymbol{K}\bar{\boldsymbol{u}}^{n}+\boldsymbol{F}^{n+1} \tag{10}$$

where the parameter β is 0.25. We note here that the load vector $\boldsymbol{F}^{n+1}$ at time step $(n+1)$ is computed through

$$\boldsymbol{F}^{n+1}=\boldsymbol{F}^{n}+\int_{\partial\Omega_1}\boldsymbol{\Phi}^T(\boldsymbol{p}^{n}-\boldsymbol{p}^{n-1})\,ds \tag{11}$$

where $\boldsymbol{p}$ indicates the time-step-wise finite element approximation of the hydrodynamic pressure computed from the Navier-Stokes system of Eqs. (4) and (5). In Eq. (10), nodal vectors of velocity and displacement at time step $(n+1)$ is updated through

$$\dot{\bar{\boldsymbol{u}}}^{n+1}=\dot{\bar{\boldsymbol{u}}}^{n}+0.5\Delta t(\ddot{\bar{\boldsymbol{u}}}^{n+1}+\ddot{\bar{\boldsymbol{u}}}^{n}) \tag{12}$$

$$\bar{\boldsymbol{u}}^{n+1}=\bar{\boldsymbol{u}}^{n}+\Delta t\dot{\bar{\boldsymbol{u}}}^{n}+(\Delta t)^2[(0.5-\beta)\ddot{\bar{\boldsymbol{u}}}^{n}+\beta\dot{\bar{\boldsymbol{u}}}^{n+1}] \tag{13}$$

In order to employ the C-fractional time integration method, we first discretize explicitly the flow equations in the ALE description, (4) and (5), according to the Crank-Nicolson scheme

$$\frac{\nu_i^{n+1}-\nu_i^{n}}{\Delta t}+(\nu_j^{*}-\hat{\nu}_j^{n})\,\nu_{i,j}^{n+\frac{1}{2}}-\frac{1}{\rho_F}\tau_{ij,j}^{n+\frac{1}{2}}=g_i \tag{14}$$

$$\nu_{i,i}^{n+1}=0 \tag{15}$$

with

$$\tau_{ij,j}^{n+\frac{1}{2}}=\mu\nu_{i,jj}^{n+\frac{1}{2}}-p_{,i}^{n+\frac{1}{2}} \tag{16}$$

$$\nu_i^{*}=\nu_i^{n+\frac{1}{2}}=(3\nu_i^{n}-\nu_i^{n-1})/2 \tag{17}$$

The relation $\nu_i^{n+1}=2\nu_i^{n}-\nu_i^{n-1}$ is used for Eq. (17). Then, Eq. (14) can be rewritten as follows:

$$\frac{\nu_i^{n+1}-\nu_i^{n}}{\Delta t}+(\nu_j^{*}-\hat{\nu}_j^{n})\,\nu_{i,j}^{n}+\frac{1}{\rho_F}p_{,i}^{n+\frac{1}{2}}-\frac{\mu}{\rho_F}\nu_{i,jj}^{n+\frac{1}{2}} -\frac{\Delta t}{2}(\nu_j^{*}-\hat{\nu}_j^{n})\,\Lambda_{i,j}^{n+\frac{1}{2}}=g_i \tag{18}$$

$$\Lambda_i^{n+\frac{1}{2}}=\left[(\nu_k^{*}-\hat{\nu}_k^{n})\,\nu_{i,k}^{n+\frac{1}{2}}+\frac{1}{\rho_F}p_{,i}^{n+\frac{1}{2}} -\frac{1}{\rho_F}\mu\nu_{i,kk}^{n+\frac{1}{2}}-g_i\right] \tag{19}$$

with the initial condition (7) and

$$\nu_i^{n+\frac{1}{2}}=\partial u_i^{n+\frac{1}{2}}/\partial t,\ \text{on}\ \partial\Omega_I \qquad \tau_{ij}^{n+\frac{1}{2}}n_j=\hat{t}_i^{n+\frac{1}{2}},\ \text{on}\ \partial\Omega_F^S \tag{20}$$

A simple replacement $(\nu_j^{*}-\hat{\nu}_j^{n})\,\nu_{i,j}^{n+\frac{1}{2}}=(\nu_j^{*}-\hat{\nu}_j^{n})\,[\nu_{i,j}^{n}+(\nu_i^{n+1}-\nu_i^{n})_{,j}/2]$, together with Eqs. (14) and (16), is employed to derive Eq. (18). Taking divergence to Eq. (14) and enforcing the continuity constraint lead to the time-step-wise pressure equation and boundary conditions given by

$$\frac{1}{\rho_F}p_{,ii}^{n+\frac{1}{2}}=\frac{1}{\Delta t}\nu_{i,i}^{n}-\left[(\nu_j^{*}-\hat{\nu}_j^{n})\,\nu_{i,j}^{n+\frac{1}{2}} -\frac{\mu}{\rho_F}\nu_{i,jj}^{n+\frac{1}{2}}-g_i\right]_{,i} \tag{21}$$

$$p^{n+\frac{1}{2}}=0,\ \text{on}\ \partial\Omega_F^S \tag{22a}$$

$$p_{,i}^{n+\frac{1}{2}}n_i=-\frac{\rho_F}{\Delta t}(\partial u_i/\partial t-\partial u_i^{n}/\partial t)\,n_i =\gamma^{n+\frac{1}{2}},\ \text{on}\ \partial\Omega_I \tag{22b}$$

Eq. (22b) is derived by the basic relation $\nabla p=-\rho_F\partial\boldsymbol{\nu}/\partial t$, together with the boundary condition (20) imposed on $\partial\Omega_I$, and $\gamma^{n+1/2}$ is the interface boundary data calculated with structure velocities.

The variational forms corresponding to the above two semi-discretized equations (18) and (21) can be obtained by introducing the virtual velocity and pressure, respectively. To which we approximate two step-wise variables using isoparametric basis functions,

$$\boldsymbol{\nu}^{n}(\boldsymbol{x})=\boldsymbol{\Phi}(\boldsymbol{x})\,\bar{\boldsymbol{\nu}}^{n},\ p^{n}(\boldsymbol{x})=\Psi(\boldsymbol{x})\,\bar{\boldsymbol{p}}^{n} \tag{23}$$

in which, $\boldsymbol{\Phi}$ are the $(3\times 3N)$ matrix and Ψ the $(1\times N)$ matrix, constructed with N basis functions. After the straightforward manipulation, we have a set of fully discretized and explicit matrix equations:

$$\boldsymbol{H}\bar{\boldsymbol{p}}^{n+\frac{1}{2}}=-\frac{1}{\Delta t}\boldsymbol{G}^T\bar{\boldsymbol{\nu}}^{n}-\boldsymbol{E}\bar{\boldsymbol{\nu}}^{n+\frac{1}{2}}+\boldsymbol{\Theta}^{n+\frac{1}{2}}+\boldsymbol{b}_P \tag{24}$$

$$\frac{1}{\Delta t}\boldsymbol{F}(\bar{\boldsymbol{\nu}}^{n+1}-\bar{\boldsymbol{\nu}}^{n})+\boldsymbol{A}\bar{\boldsymbol{\nu}}^{n}-\boldsymbol{G}\bar{\boldsymbol{p}}^{n+\frac{1}{2}}+\boldsymbol{L}\bar{\boldsymbol{\nu}}^{n+\frac{1}{2}} +\frac{\Delta t}{2}\left(\boldsymbol{Q}\bar{\boldsymbol{\nu}}^{n+\frac{1}{2}}+\boldsymbol{R}\bar{\boldsymbol{p}}^{n+\frac{1}{2}}-\boldsymbol{S}\right)=\boldsymbol{\Gamma}^{n+\frac{1}{2}}+\boldsymbol{b}_V \tag{25}$$

The matrices in above equations are defined in Appendix. It is worthy noting that the mesh velocity $\hat{\boldsymbol{\nu}}^{n}$ in the matrices is determined in the remeshing and smoothing processes.

4. Remeshing and Smoothing

Referring to Fig. 2, the remeshing in our study is performed basically through three steps: (S1) take $\hat{\boldsymbol{v}}^n=\boldsymbol{v}^*$ for the whole nodes, and next (S2) smooth the relocated mesh, if required. Here, the second step is iteratively carried out and split into two steps again: (S2-1) smooth first the boundary nodes, and (S2-2) smooth the interior nodes. Of course, step (S1) is identical to the remshing in the Lagrangian approach. When we denote $\boldsymbol{x}_A^c$ be the current location of free-surface node A before remeshing, its new location $\boldsymbol{x}_A^0$ after step (S1) will be

$$\boldsymbol{x}_A^0=\boldsymbol{x}_A^c+\hat{\boldsymbol{v}}_A^n\Delta t \tag{26}$$

with the mesh velocity $\boldsymbol{v}_A^0=\hat{\boldsymbol{v}}_A^n$. Updating all free-surface nodes generates a new mesh X_m^0.

We next decide whether the smoothing is necessary or not, according to the decision criterion described later, and we perform the iterative smoothing procedure if necessary. For our study, we employ the simple averaging method in which the location of node A is smoothed by averaging the geometric locations of m_A surrounding nodes. Referring to Fig. 2(b), the surrounding nodes of a boundary node A are composed of the boundary nodes of the elements sharing node A. The free-surface coordinates $\boldsymbol{x}^0$ and mesh velocities $\boldsymbol{v}^0$ of all supporting elements can be mapped into a 2D bilinear master element. We first smooth two tangential coordinate components (on the free surface) of node A using the iterative simple averaging method:

$$(x_\alpha)_A^l=(x_\alpha)_A^{l-1}+\frac{1}{m_A}\sum_{M=1}^{m_A}(x_\alpha)_M,\quad \alpha=t_1,\ t_2 \tag{27}$$

where (and hereafter) l refers to the iteration cycle ($l=1, 2, 3, \cdots$). While the vertical coordinates $(x_n)_A$ of the surface nodes after the surface smoothing can be interpolated from the surface geometry before the surface smoothing. Then, we obtain the final location $\boldsymbol{x}_A^F$ of boundary node A to be moved and the corresponding mesh velocity $\hat{\boldsymbol{v}}_A^n=\boldsymbol{v}^0(\boldsymbol{x}_A^F)$ from the velocity mapping function.

On the other hand, the surrounding nodes of any interior node A are all nodes (except for the node A itself) of the elements sharing the node A. Then, the location of node A is updated through

$$\boldsymbol{x}_A^l=\boldsymbol{x}_A^{l-1}+\frac{1}{m_A}\sum_{M=1}^{m_A}\boldsymbol{x}_M \tag{28}$$

Then, the final location of interior node A to be moved is $\boldsymbol{x}_A^F=\boldsymbol{x}_A^l$ with its final velocity $\hat{\boldsymbol{v}}_A^n=\boldsymbol{v}_A^0+(\boldsymbol{x}_A^F-\boldsymbol{x}_A^c)/\Delta t$. After we smooth all surface and interior nodes, we calculate the total liquid volume of the mesh and compare the initial fuel volume to calculate the volume change ΔV. In order to avoid the volume change accumulation along the time incremental process, we correct the vertical coordinates of all free-surface nodes according to

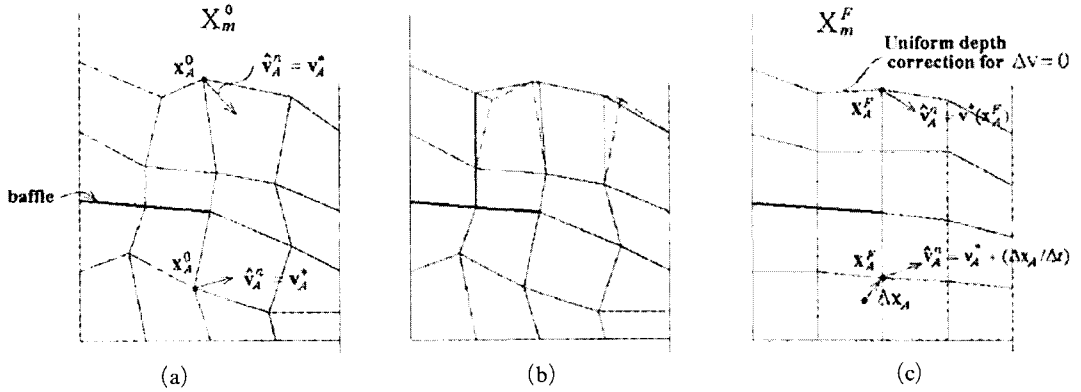

Fig. 2 Three-step mesh update procedure (2D representation)

$$(x_n)_A^F=(x_n)_A^F-\Delta V/Area(\partial\Omega_F^S) \quad (29)$$

This completes the remeshing step to obtain the final mesh X_m^F with the updated nodal coordinates $\boldsymbol{x}_A^F$ and the mesh velocity $\hat{\boldsymbol{v}}^n$, as depicted in Fig. 2(c), which is required for the next-step ALE computation.

5. Numerical Experiment

Figure 3(a) depicts a model container in uniform horizontal motion with v of 60 m/sec where fuel occupies 50% of the total container volume. The container is forced to subject a yawing perturbation such that it rotates right and left according to a yawing cycle : $-5.73^o \rightarrow +11.46^o \rightarrow +5.73^o$ about the z-axis with uniform angular velocity $|\omega_Z|=5.0$ rad/sec, as illustrated in Fig. 3(b). Reminding that a yawing cycle takes 0.08 sec, we simulate the yawing motion during 0.2s in order for the sufficient investigation of the dynamic response. Meanwhile, we intend to examine two moment resultants M_X and M_Z, and three force resultants F_X, F_Y and F_Z. In fact, the moment resultant M_Y (i.e. the rolling moment) is not significant in yawing perturbation.

We record geometry and material data taken for our numerical experiments in Table 1, in which the baffle number, the installation location and the inner-hole diameter are taken variable for the parametric investigation. Regarding the baffle number and the installation location, we consider three cases : 0, 1 and 2 with uniform spacing. On the other hand, we consider four cases for the relative inner-hole diameter D_B/D : 0.75, 0.5, 0.25 and 0.125. It is worth to mention that linear and angular velocities are numerically implemented by specifying the time-stage-wise linear and angular displacements along the edges of two side plates.

Figure 4(a) and 4(b) represent finite element meshes of structure and fuel, respectively, for which 1,760 four-node shell elements and 4,580 three-dimensional trilinear solid elements are used. Even though total element numbers of structure and fuel meshes vary according to the choice of the baffle number and the inner-hole diameter, the relative change in total element number is not significant. On the other hand, the speed of sound in fuel is found to be 1,640 m/sec from the fuel density and the bulk modulus given in Table 1. According to the elementary dynamics,

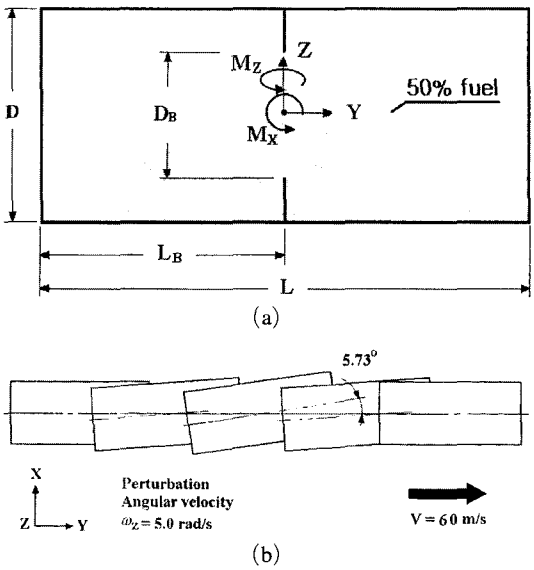

Fig. 3 Model problem description : (a) Model container and dynamic resultants ; (b) Yawing condition

Table 1 Geometry and material data taken for the numerical simulation

	Material data		Geometry data (m)	
Structure	Density ρ_S(kg/m^3)	2.78×10^3	Diameter of tank D	0.4
	Young's modulus E(N/m^2)	7.24×10^{10}	Length of tank L	1.0
	Poisson's ratio ν	0.33	Structure thickness t	0.00254
	Yield strength σ_Y(N/m^2)	4.85×10^8	Baffle thickness t_B	0.003
Fuel	Density ρ_F(kg/m^3)	8.15×10^2	Relative fuel amount	50%
	Bulk modulus κ(N/m^3)	2.2×10^9	Inner-hole size D_B	variable
	Kinematic viscosity μ(kg/m·s)	8.15×10^{-4}	Baffle spacing L_B	uniform

we also found that the peak flow velocity does not exceed 100 m/sec within the observation time period. Then, according to the Courant criterion $(\Delta t)_{crit} \leq h/(c+u)$, the initial fluid mesh shown in Fig. 4(b) with the smallest mesh size requires the critical time-step size $(\Delta t)_{crit}$ of 1.09×10^{-5} sec. It is worthy noting that the smoothing scheme described in Section 4 exhibits rapid convergence speed so that the smoothing process satisfying the preset tolerance is completed in a few iterations.

Fuel flow patterns within container without and with a baffle at three subsequent time stages are presented in Fig. 5. The fluctuation of fuel free surface to the left and right as well as the internal fuel flow is shown to be severe with the lapse of time. For this simulation during 0.2 sec after yawing perturbation, almost 45,000 time iterations are taken. And, the extreme fuel mesh distortion was successfully adjusted according to the mesh smoothing process described above. Meanwhile, the free surface fluctuation becomes remarkably suppressed when a baffle is inserted at the center, and which confirms the effectiveness of baffle as a dynamic damping device for moving fuel container.

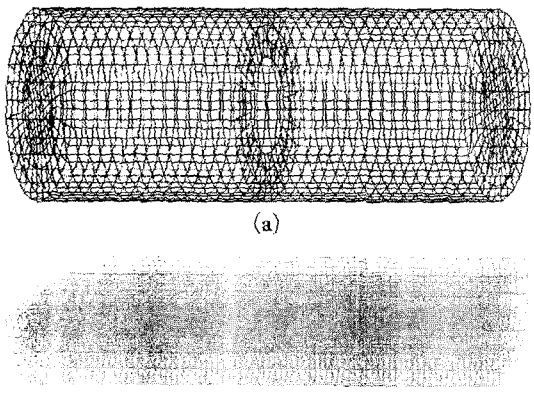

Fig. 4 Finite element meshes : (a) Structure ; (b) Fuel

However, we can not see the considerable improvement in the suppression of free surface fluctuation for the two-baffle case compared to the one-baffle case. A particular feature in the two-baffle case is that the fuel free surface between two baffles keeps stable without any remarkable fluctuation. The parametric effects of baffle on the dynamic pressure resultants exerting on the container are given below.

Time history responses of three force resultants and two moment resultants to the baffle number are presented in Fig. 6 and Fig. 7, respectively. As a whole, all of five resultants show the peak response near 0.025 sec after the yawing perturbation, regardless of the baffle number. This point of time is when the container starts to return to the horizontal position after the first yawing perturbation to the left, referring to Fig. 3(b),

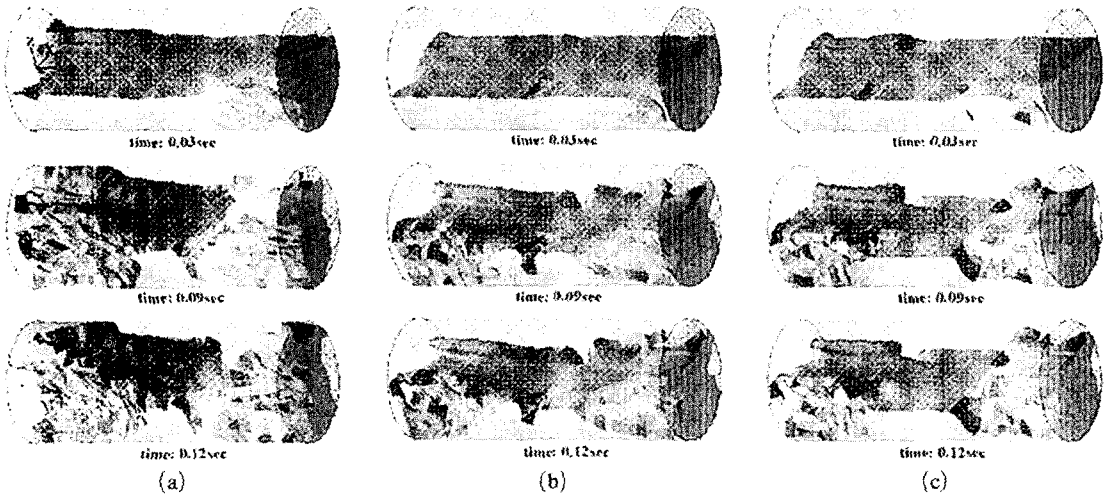

Fig. 5 Free surface fluctuation of fuel : (a) Without baffle ; (b) With one baffle ; and (c) With two baffle

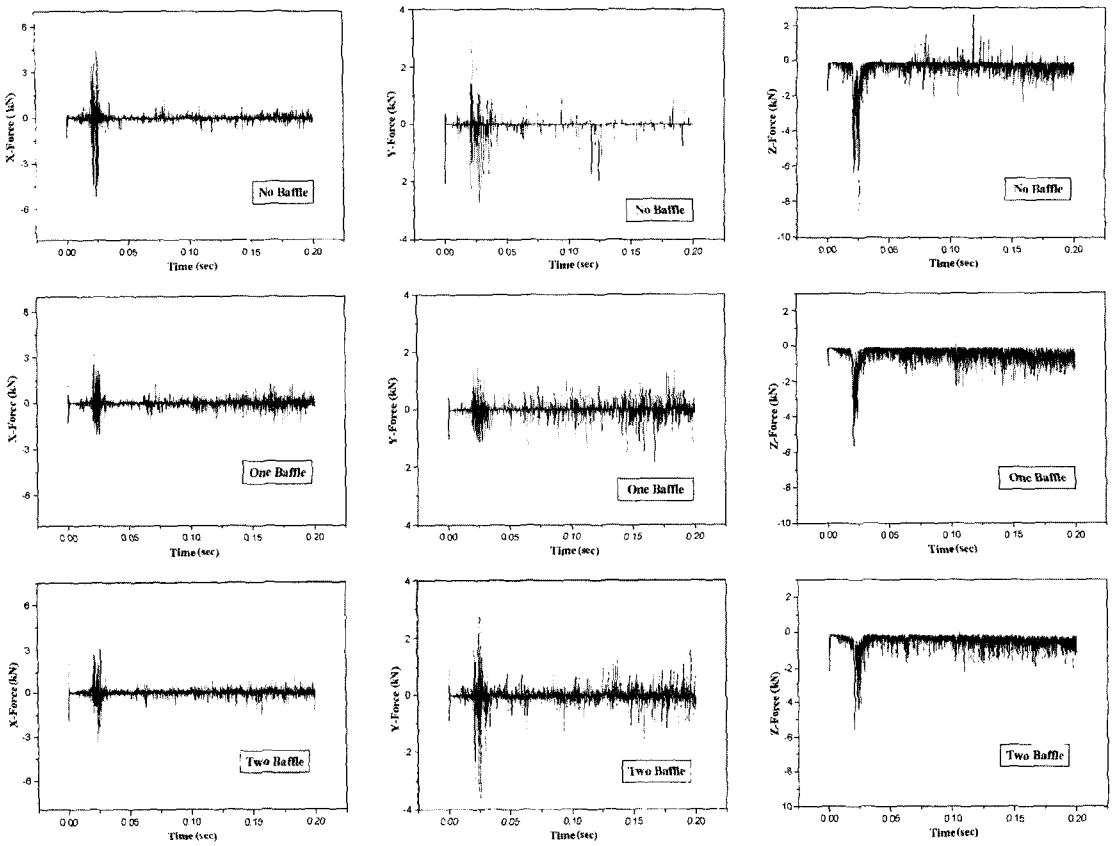

Fig. 6 Hydrodynamic force resultants to the baffle number: (a) x-force; (b) y-force; and (c) z-force

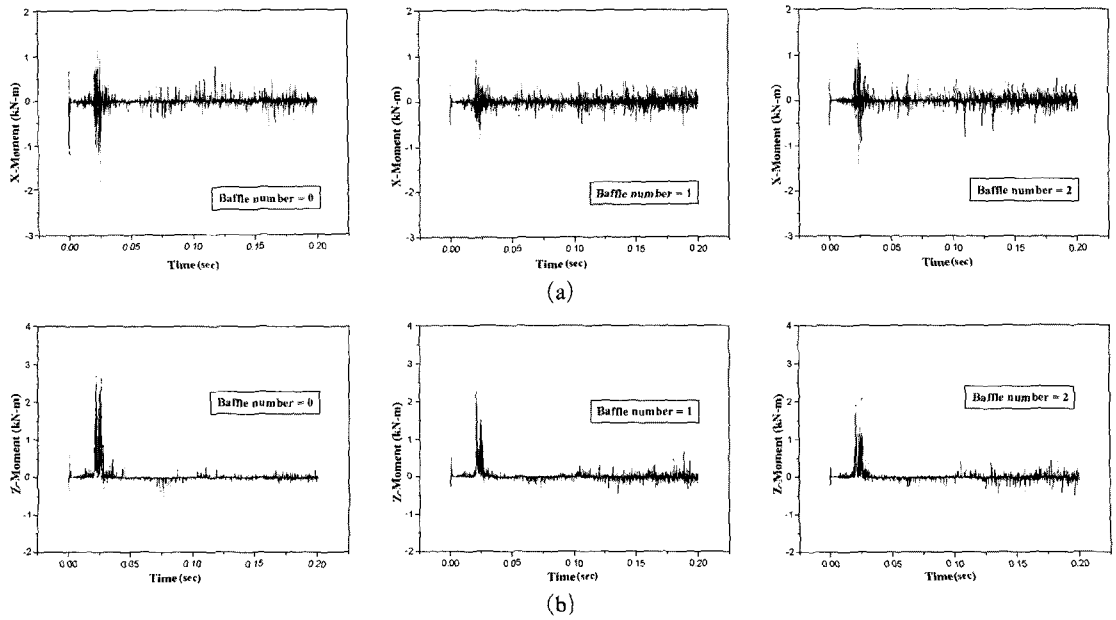

Fig. 7 Hydrodynamic moment resultants to the baffle number: (a) x-moment; (b) z-moment

so the peak response occurrence is natural. Regarding to the baffle number, the peaks of all five resultants are lowest when one baffle is installed. For the two-baffle case, all resultants except for the z-moment become higher than the one-baffle case, still more some of resultants become worse than the no-baffle case. The parametric variations of the peaks of five resultants to the baffle number are given in Fig. 8(a) and 8(b). This implies that the dynamic suppression for the fuel container in yawing perturbation is not monotonically improved in proportional to the baffle number.

For the one-baffle case showing the best dynamic damping effect, we performed the parametric investigation by varying the baffle inner-hole diameter. The parametric variations of the peaks of three force resultants and two moment resultants are presented in Figs. 9(a) and 9(b), respectively. Except for the z- and x-moments, four resultants produce the lowest peaks when the relative inner-hole diameter D_B/D is 0.5, with the convex-like variation in the peak response. For the two exceptional components the parametric variation near this inner-hole diameter is not remarkable so that the recommendable inner-hole diameter is a half of the container diameter. We infer that the fuel flow suppression decreases as the inner-hole diameter increases while the frictional resistance increases with the inner-hole size decrease.

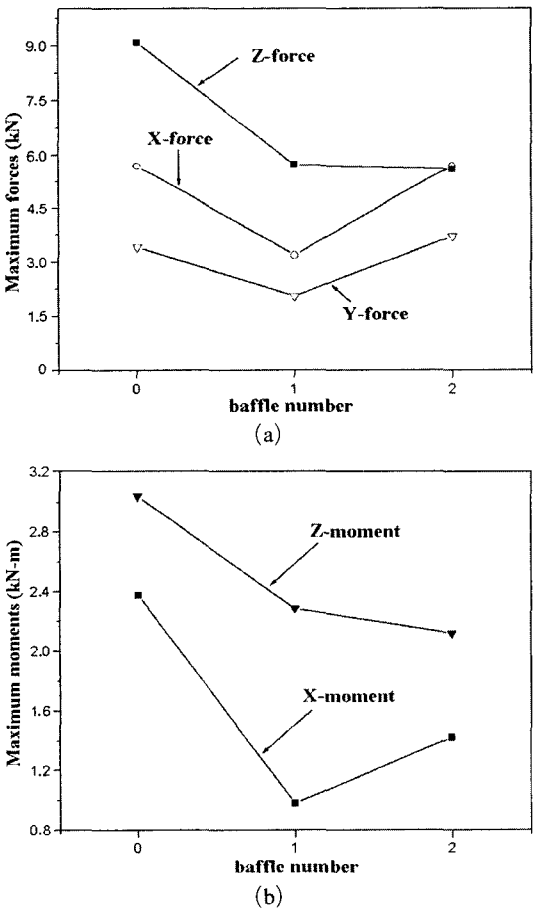

Fig. 8 Variations to the baffle number: (a) Maximum forces; (b) Maximum moments

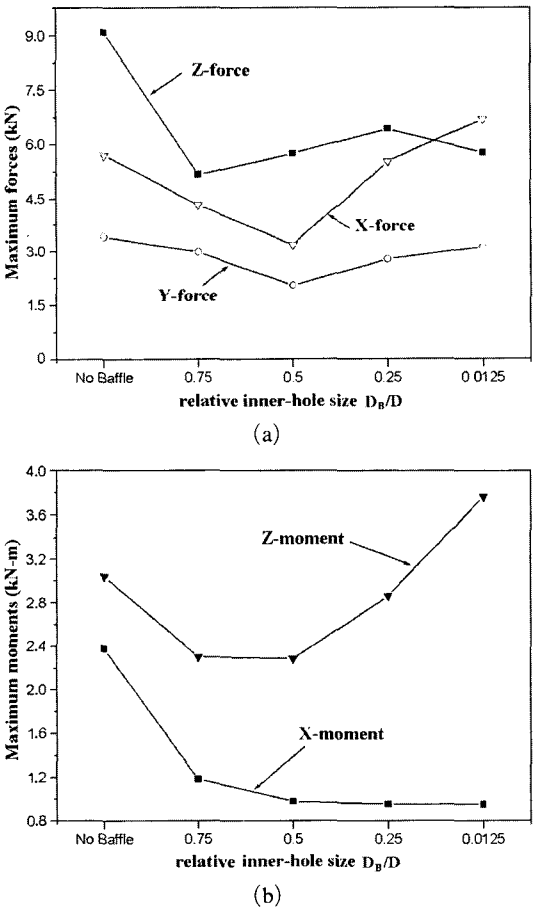

Fig. 9 Variations to the baffle inner-hole diameter: (a) Maximum forces; (b) Maximum moments

6. Conclusion

An ALE finite element method for the structural dynamic analysis of baffled fuel container was presented. The fluid mesh smoothing according to an iterative geometric averaging algorithm successfully resolved the excessive mesh distortion caused by the complex fuel flow. The necessity of smoothing process was judged by comparing the critical time step size evaluated by the Courant criterion with the preset allowable value, and which achieved both the numerical stability and the minimum CPU time. The coupled fluid-structure time integration was performed iteratively by the implicit Newmark method and the explicit fractional method so that the critical time step size was determined by the fluid mesh parameters. From the numerical experiments, we found that the dynamic response of baffled cylindrical fuel container becomes more stable that the case without baffle, but its improvement is not simply proportional to the baffle number. Meanwhile, the relative inner-hole diameter produces on the whole the best damping effect when D_B/D is 0.5.

Acknowledgment

WSY would like to thank the Ministry of Science and Technology of Korea for the financial support by a grant (M1-0203-00-0017-02J0000-00910) under the NRL (National Research Laboratory). And, the financial support for this work by the Korea Industrial Technology Foundation (KOTEF) (2003. 6-2006. 4) is gratefully acknowledged.

References

Abramson, H. N., 1966, T*he Dynamic Behavior of Liquids in Moving Containers*, NASA SP-106.

Bathe, K. J., 1996, *Finite Element Procedures*, Prentice-Hall, Singapore.

Bauer, H. F., 1966, "Nonlinear Mechanical Model for the Description of Propellant Sloshing," *AIAA Journal*, Vol. 4, No. 9, pp. 1662~1668.

Belytschko, T. and Kennedy, J. M., 1978, "Computer Models for Subassembly Simulation," *Nucl. Engrg. Des.*, Vol. 49, pp. 17-38.

Benson, D. J., 1989, "An Efficient, Accurate, Simple ALE Method for Nonlinear Finite Element Programs," *Comput. Methods Appl. Mech. Engrg.*, Vol. 72, pp. 305~350.

Cho, J. R. and Song, J. M., 2001, "Assessment of Classical Numerical Models for the Separate Liquid-Structure Modal Analysis," *J. Sound and Vibration*, Vol. 239, No. 5, pp. 995~1012.

Chorin, A. J., 1968, "Numerical Solution of the Navier-Stokes Equations," *Mathematics of Computation*, Vol. 22, pp. 745~762.

Donea, J., Giuliani, S. and Halleux, J. P., 1982, "An arbitrary Lagrangian-Eulerian Finite Element Method for Transient Dynamic Fluid-Structure Interactions," *Comput. Methods Appl. Mech. Engrg.*, Vol. 33, pp. 689~723.

Hayashi, M., Hatanaka, K. and Kawahara, M., 1991, "Lagrangian Finite Element Method for Free Surface Navier-Stokes Flow Using Fractional Step Methods," *Int. J. for Numerical Methods in Fluids*, Vol. 13, pp. 805~840.

Hirt, C. W., Amsden, A. A. and Cook, J. L., 1974, "An Arbitrary Lagrangian-Eulerian Computing Method for all flow Speeds," *J. Computational Physics*, Vol. 14, pp. 227~253.

Hughes, T. J. R., Liu, W. K. and Zimmerman, T. K., 1981, "Lagrangian-Eulerian Finite Element Formulation for Incompressible Viscous Flows," *Comput. Methods Appl. Mech. Engrg.*, Vol. 58, pp. 227~245.

Kennedy, J. M. and Belytschko, T. B., 1981, "Theory and Application of a Finite Element Method for Arbitrary Lagrangian-Eulerian Fluids and Structures," *Nucl. Engrg. Des.*, Vol. 68, pp. 129~146.

Miyata, T., Yamada, H. and Saito, Y., 1988, "Suppression of Tower-Like Structure Vibration by Damping Effect of Sloshing Water Contained," *Trans. Japan Society of Civil Engineering*, Vol. 34A, pp. 617~626.

Newmark, N. M., 1959, "A Method of Computation for Structural Dynamics," *ASCE Journal of Engineering Mechanics Devision*, Vol. 85, pp. 67~94.

Paidoussis, M. P., 1998, *Fluid-Structure In-*

teractions : Slender Structures and Axial Flow, Vol. 1, Academic Press, New York.

Welt, F. and Modi, V. J., 1992, "Vibration Damping Through Liquid Sloshing, Part 2 : Experimental Results," *J. Vibration and Acoustics*, Vol. 114, pp. 17~23.

Appendix : Definition of Matrices

By defining the divergence-like operator $\boldsymbol{D}$ by $\{\partial/\partial x, \partial/\partial y, \partial/\partial z\}^T$, together with Eq. (23), we can easily derive

$$(\boldsymbol{s}\cdot\nabla)\boldsymbol{\nu}=(\bar{\boldsymbol{s}}^{nT}\boldsymbol{B}^T\boldsymbol{I})\boldsymbol{\Phi}\bar{\boldsymbol{\nu}},\ \boldsymbol{B}=\boldsymbol{D}^T\boldsymbol{\Phi} \tag{A1}$$

Here, $\boldsymbol{I}$ denotes the (3×3) identity matrix, and $\bar{\boldsymbol{s}}^n$ the step-wise nodal vector of the convection velocity $(\boldsymbol{\nu}^*-\hat{\boldsymbol{\nu}}^n)$. Then, the five matrices in Eq. (24) are defined by

$$\boldsymbol{H}=\int_{\Omega_F}\frac{1}{\rho_F}(\nabla\Psi)^T\nabla\Psi\,dV \tag{A2}$$

$$G=\int_{\Omega_F}\boldsymbol{B}^T\Psi\,dV \tag{A3}$$

$$E=\int_{\Omega_F}(\nabla\Psi)^T(\bar{\boldsymbol{s}}^{nT}\boldsymbol{B}^T\boldsymbol{I})\,\Phi\,dV \tag{A4}$$

$$\Theta^{n+\frac{1}{2}}=\int_{\partial\Omega_I}\Psi^T\gamma^{n+\frac{1}{2}}\,ds \tag{A5}$$

$$\boldsymbol{b}_P=\int_{\Omega_F}(\nabla\Psi)^T\boldsymbol{g}\,dV \tag{A6}$$

Additionally, we define $\tilde{\boldsymbol{B}}=\tilde{\boldsymbol{D}}^T\boldsymbol{\Phi}$ by denoting $\tilde{\boldsymbol{D}}^T$ the (9×3) differential operator expressing the (9×1) vector of $\nabla\boldsymbol{\nu}$. Then, the remaining matrices in Eq. (25) are as follows :

$$\boldsymbol{F}=\int_{\Omega_f}\boldsymbol{\Phi}^T\boldsymbol{\Phi}\,dV \tag{A7}$$

$$\boldsymbol{A}=\int_{\Omega_F}\boldsymbol{\Phi}^T(\bar{\boldsymbol{s}}^{nT}\boldsymbol{B}^T\boldsymbol{I})\,\Theta\,dV \tag{A8}$$

$$\boldsymbol{L}=\int_{\Omega_F}\frac{\mu}{\rho_G}\tilde{\boldsymbol{B}}^T\tilde{\boldsymbol{B}}\,dV \tag{A9}$$

$$\boldsymbol{Q}=\int_{\Omega_F}\boldsymbol{\Phi}^T(\bar{\boldsymbol{s}}^{nT}\boldsymbol{B}^TI)^T(\bar{\boldsymbol{s}}^{nT}\boldsymbol{B}^T\boldsymbol{I})\,\Phi\,dV \tag{A10}$$

$$\boldsymbol{R}=\int_{\Omega_F}\boldsymbol{\Phi}^T(\bar{\boldsymbol{s}}^{nT}\boldsymbol{B}^TI)^T\nabla\Psi\,dV \tag{A11}$$

$$\boldsymbol{S}=\int_{\Omega_F}\boldsymbol{\Phi}^T(\bar{\boldsymbol{s}}^{nT}\boldsymbol{B}^TI)^T\boldsymbol{g}\,dV \tag{A12}$$

$$\Gamma^{n+\frac{1}{2}}=\int_{\Omega_F}\boldsymbol{\Phi}^T\hat{\boldsymbol{t}}^{n+\frac{1}{2}}ds \tag{A13}$$

$$\boldsymbol{b}_V=\int_{\Omega_F}\boldsymbol{\Phi}^T\boldsymbol{g}\,dV \tag{A14}$$